Strain-induced in situ formation of NiOOH species on Co—Co bond for selective electrooxidation of 5-hydroxymethylfurfural and efficient hydrogen production

Zhaoyu Zhou [a], Ya-nan Xie [a], Lingzhi Sun [a], Zhiming Wang [a], Weikang Wang [a], Luozhen Jiang [c], Xin Tao [c], Lina Li [c,*], Xin-Hao Li [b,*], Guohua Zhao [a,*]

[a] School of Chemical Science and Engineering, Key Laboratory of Spine and Spinal Cord Injury Repair and Regeneration, Ministry of Education, Tongji Hospital, Tongji University, Shanghai, 200092, China
[b] School of Chemistry and Chemical Engineering, Shanghai Jiao Tong University, Shanghai 2000240, China
[c] Shanghai Synchrotron Radiation Facility, Shanghai Advanced Research Institute, Shanghai 201800, China

ARTICLE INFO

ABSTRACT

It is an efficient strategy to replace sluggish water oxidation with a thermodynamically more favorable reaction, electrochemical selective conversion of 5-hydroxymethylfurfural (HMF) to 2,5-furandicarboxylic acid (FDCA), to promote hydrogen production. High selectivity and Faradaic efficiency ($>99\%$) for the conversion of HMF to FDCA and simultaneous hydrogen production were achieved under 220 mV overpotential on $NiCo_2O_4$ electrode. The addition of HMF decreased the anode overpotential, and the amount of generated hydrogen through coupling with HMF oxidation is 8.16 times higher than that of water splitting. Operando Raman identified that NiOOH as the main active species for selective electrooxidation of HMF to FDCA. Operando EXAFS demonstrates that the crystal-strain induced formation of NiOOH from Co—Co bond and such a crystal strain could be further enhanced by the electric field for the in situ formation of more NiOOH. The accelerated reaction pathway was confirmed by operando electrochemical infrared (EC-IR) and DFT calculations.

1. Introduction

The increasing environmental pollution and depletion of fossil fuels have motivated considerable efforts to develop green and eco-friendly clean energy storage and conversion technologies [1–6]. As a renewable alternative to traditional fossil fuels, biomass platform molecules (exemplified with 5-hydroxymethylfurfural (HMF) here) can be further upgraded into high value-added chemicals derivatives 2,5-furandicarboxylicacid (FDCA) for the production of polyamides, polyurethanes and polyesters [7–14]. Traditionally, the selective conversion of HMF to FDCA was performed at elevated temperatures (30–130 °C) and high pressures of oxygen gas (e.g., 0.3–2.0 MPa) by using noble-metal-based catalysts (e.g., Au, Pt, Ru, and Pd) [15–22]. Therefore, exploration of sustainable methods for the up-gradation of these biomass molecules is still highly required for real applications.

Recently, electrochemical dehydrogenation of HMF could also be used to produce FDCA and hydrogen energy with very high atomic economics [20,23,24]. The selectivity was controlled by the potential,

and it can avoid the use of O_2 or other dangerous chemical oxidants. Additionally, the calculated Gibbs free energy for the overall reaction of $HMF + H_2O \rightarrow FDCA + H_2$ at room temperature is only 65.62 kJ mol^{-1}, which is smaller than overall water splitting (237.129 kJ mol^{-1}) [10,25, 26]. Moreover, this anodic half-reaction of HMF oxidation into FDCA provides six electrons that are possible to be fully utilized for cathodic hydrogen production.

Some related researches have also been performed, while much effort has been focused on designing powerful and cheap electrode materials to improve the conversion efficiency and selectivity of HMF [27–31]. For example, the effect of the Pd, Au and alloys on the electrochemical oxidation of HMF was investigated, but the highest selectivity for FDCA was only 83% [27]. Subsequently, Choi reported that photoelectrocatalytic selective conversion of HMF to FDCA with nearly 100% Faradaic efficiency at 1.54 V (vs. RHE). However, 2,2,6,6-tetramethylpiperidine-1-oxyl (TEMPO) was selected as the redox mediator, which resulted in a high separation cost [12]. Recently, transition metal-based materials (Fe, Co, Ni, and Cu) were widely used for the

---

selective oxidation of HMF to FDCA and simultaneous hydrogen production because of the unique e_g orbital hybridization and abundant 3d electron number. Cobalt-based spinel catalysts of $NiCo_2O_4$ and Co_3O_4 with filamentous nanoarchitecture were designed for electrochemical conversion of HMF to FDCA, which showed 99.6% HMF conversion efficiency with 90.8% selectivity of FDCA. The selectivity and conversion rate of HMF to FDCA has been greatly improved [32]. Additionally, Ni-based materials (e.g., Ni_3S_2, Ni_2P, S-Ni@C, Ni/CdS and Ni/CP) exhibited high activity and Faradaic efficiency by modulating the electronic structure of Ni [33–37]. It was found that the HMF oxidation performance of Ni_3S_2/NF was higher than that of commercially available NiC, NiO, and NiS catalysts [38]. Additionally, high-entropy oxides were also utilized for HMF electrooxidation. The quinary $(FeCrCoNiCu)_3O_4$ nanosheets with abundant oxygen vacancies and high surface area was synthesized through a low-temperature plasma strategy, which showed the lower onset potential and faster kinetics for HMF oxidation [39]. Besides, operando surface-enhanced Raman spectroelectrochemical technology was used to explore the electrode material transformation and surface reaction intermediates under an applied voltage by constructing core-shell gold-metal oxide AuNi nanostructures electrode, and NiOOH was identified as the active species for electrochemical conversion of HMF to FDCA [40]. Recently, $NiO-Co_3O_4$ nanosheets electrocatalysts have drawn substantial attention to the HMF selective conversion, and it was identified that the real active species was NiOOH [41]. Additionally, some studies confirmed that the Co substitution can promote the formation of NiOOH and enhance the selective oxidation of HMF into FDCA in the NiCoP electrode [42]. Though the Ni/ NiOOH was utilized for electrochemical FDCA production based on a flow reactor, only 89% yield of FDCA and 80% Faradaic efficiency were achieved [43]. Therefore, it is more conducive to selective electrooxidation of HMF to FDCA through in situ production of NiOOH active species in Ni-based materials. However, the driven forces for NiOOH formation in these Ni-based precatalysts are still not clear at the moment [44–46]. Therefore, an in-depth study of the NiOOH in situ formation mechanism is of great significance for the design of NiOOH-rich catalysts for the highly efficient transformation of HMF into FDCA.

In this work, a series of $Ni_xCo_{3-x}O_4$ electrodes with different crystal structures were prepared. The $Ni_xCo_{3-x}O_4$ showed different Co—Co bond lengths. We regulate the Co—Co bond length by adjusting the ratios of Ni and Co. The effect of Co—Co bond strain or stretch relative to Co_3O_4 on the formation of NiOOH in the $Ni_xCo_{3-x}O_4$ electrodes was investigated in detail. We successfully identified the key role of the Co—Co bond strain of $Ni_xCo_{3-x}O_4$ materials in initiating the formation of NiOOH species as the active components for selective conversion of HMF to FDCA. The in situ formation of NiOOH in well-designed $Ni_xCo_{3-x}O_4$ materials as identified by operando electrochemical Raman and extended X-ray absorption fine structure spectroscopy (EXAFS) technologies confirmed that the strain of Co—Co bond affects the formation of NiOOH. As the increased strain of the Co—Co bond, more NiOOH was formed. The potential can induce further strain of the Ni—O bond, which leads to the in situ formation of NiOOH. The $NiCo_2O_4$ materials with the shortest Co—Co bonds are more sensitive to the working voltage and thus generate more NiOOH species under fixed conditions, providing excellent performance (>99% selectivity and Faradaic efficiency) and simultaneous hydrogen production (0.986 mmol cm^{-2}, 8.16 times of overall water splitting). The reaction pathway of the selective conversion of HMF to FDCA was further confirmed by operando electrochemical infrared (EC-IR) and Density functional theory (DFT) calculations. In general, this work reveals a simple, green, and atom-economic novel approach.

2. Experiment section

2.1. Preparation of NiCo₂O₄ electrode

The $NiCo_2O_4$ nanowire loaded on nickel foam (NF) substrate was synthesized via a simple hydrothermal method according to the literature [32,47,48]. Typically, a piece of commercial NF (1.5 cm * 5 cm) was washed by sonication sequentially with 3 M HCl, distilled water, acetone and ethanol for 30 min, respectively. The ratio of cobaltous nitrate hexahydrate (1 mmol), nickel nitrate hexahydrate, urea and ammonium fluoride were 1:2:6:15. Then, deionized water (30 ml) was added and magnetically stirred for 20 min. The solution and a piece of cleaned NF were placed into a Teflon-lined stainless-steel autoclave and heated at 120 ºC for 6 h, and then it was thoroughly washed with ethanol and deionized water after the reaction, followed by drying at 70 °C overnight. Subsequently, it was annealed at 350 ºC under argon gas atmosphere for 3 h to obtain $NiCo_2O_4$ nanowires electrode. The final catalyst loading on NF was ~5.8 mg cm^{-2}. The different crystal structure electrodes were prepared by adjusting the ratio of nickel nitrate hexahydrate and cobaltous nitrate hexahydrate to 1:0, 0:1, 1:1, and 2:1 to obtain the NiO, Co_3O_4, $Ni_{1.5}Co_{1.5}O_4$ and Ni_2CoO_4 electrodes, respectively.

2.2. Materials characterization

Field emission scanning electron microscopy (FE-SEM, Hitachi S-4800, Hitachi, Japan) and high-resolution transmission electron microscopy (HR-TEM, 2100, JEOL, Japan) were used to characterize the surface morphology of the as-prepared electrodes. The crystalline structures, elemental composition and chemical states of the sample were determined by X-ray diffraction (XRD, D8 Focus X-ray diffractometer, Bruker, Germany) using Cu Kα radiation (λ = 1.540598 Å) 40 kV, 40 mA, 2° min-1) and X-ray photoelectron spectroscopy (XPS, AXIS Ultra HSA, Kratos Analytical Ltd., UK. with a monochromated Al Kα X-ray source). For XPS, all the peaks were calibrated by reference to the C1s spectrum at the binding energy of 284.7 eV. An operando electrochemical Raman spectrometer (Renishaw Crop., UK 532 nm laser) was used to determine the active species in the electrochemical HMF oxidation process. An operando electrochemical Fourier transform infrared spectroscopy (FTIR, Nicolet 8700, Thermo Fisher Scientific Inc. USA) was used to investigate the reaction intermediates for the conversion of HMF to FDCA at different times and potentials. X-ray absorption spectra (XAS) were collected with Si (111) crystal monochromators at the BL11B Beamline at Shanghai Synchrotron Radiation Facility (SSRF) (Shanghai, China).

2.3. Electrochemical characterization

The electrochemical characterization was performed in a three-electrode setup (CHI660C electrochemical station, CH Instruments Inc., USA). The working electrode ($NiCo_2O_4$), counter electrode (platinum foil) and reference electrodes (Hg/HgO) were placed in a self-made cell. The polarization curves were recorded by linear sweep voltammetry (LSV, 1 M KOH, 5 mV s^{-1}), and the potentials were converted to a reversible hydrogen electrode (RHE) according to the Nernst equation: E (vs. RHE) = E(Hg/HgO) + 0.095 + 0.059 × pH. For comparison, 10 mM HMF was added for the LSV testing. Electrochemical impedance spectroscopy (EIS) was performed in the frequency range from 10^5 Hz to 10^{-3} Hz.

2.4. Quantitative product analysis

The electrochemical selective oxidation of HMF and simultaneous hydrogen production was carried out in a double chamber reactor with a Nafion 117 proton exchange membrane at room temperature. $Ni_xCo_{3-x}O_4$ as working electrode, Pt plate as counter electrode and Hg/HgO

as the reference electrode. The electrolyte was 33 ml 1 M KOH solution containing 10 mM HMF. The working areas of the anode were 3 cm^2. 10 μL of the electrolyte solution was taken from the cell every 20 C and then 490 μL water was added to reduce the concentration for HPLC (Aglient 1260, C18 chromatography 4.6 × 100 nm, 3.5 μm) analysis quantitatively. The test conditions were as follows: the UV detector wavelength λ = 265 nm, and the separation was accomplished using an eluent consisting of 90% 10 mM NH$_4$F and 10% CH$_3$OH with 1 ml min^{-1}. The HMF conversion ratio (%) and products yield (%) was calculated as follows:

$$HMF\ conversion\ (\%) = \frac{mol\ of\ HMF\ consumed}{mol\ of\ initial\ HMF} \times 100\%$$

$$products\ yield\ (\%) = \frac{mol\ of\ product\ formed}{mol\ of\ initial\ HMF} \times 100\%$$

The Faradaic efficiency of FDCA and hydrogen production was calculated as follows:

$$FE\ (\%) = \frac{mol\ of\ FDCA\ formed}{total\ charge\ passed/(F \times 6)} \times 100\%$$

$$FE\ (\%) = \frac{mol\ of\ Hydrogen\ formed}{total\ charge\ passed/(F \times 2)} \times 100\%$$

The Faraday constant of F is 96,485 C mol^{-1}. The product of FDCA was precipitated by the addition of HCl until pH 2 and filtration and recrystallization for higher purity. Additionally, these intermediates were identified by NMR spectra, and the purification process was based on literature methods [49]. The qualitative and quantitative test of hydrogen production was via headspace gas chromatography (Shimadzu GC-2014C, TCD detector).

2.5. Density functional theory calculations

Density functional theory had been used to determine the standard potential of the HMF oxidation to FDCA with the projector augmented wave (PAW) method. The generalized gradient approximation (GGA) of the Perdew-Burke-Ernzerhof (PBE) functional is employed to deal with the exchange-functional. 400 eV was set for the energy cut-off of the plane wave basis expansion. We set the force on each atom less than 0.05 eV /Å as the convergence criterion for geometric relaxation. A 3 × 3 × 1 Monkhorst and Pack k-point sampling was utilized in our calculation for the surface structure.

2.6. Operando electrochemistry infrared spectroscopy measurement

First, 5 mg NiCo$_2$O$_4$ samples were dispersed in 1 ml containing 49:49:2 vol% water, ethanol, Nafion for ultrasonic dispersion 1 h. Then the mixture was coated on a polished glassy carbon electrode surface and dried at room temperature. The operando EC- IR cell was designed with a CaF$_2$ window (25 mm in diameter, 2 mm thickness). The Catalyst coated glassy carbon (working electrode) Pt wire (counter electrode) and Hg/HgO (reference electrode) were placed in EC-IR cell. Before testing, the working electrode was immersed in a 15 ml electrolyte containing 0.1 M HMF and 0.1 M KOH for operando electrochemical IR spectrum experiments (Nicolet 8700, Thermo Fisher Scientific Inc. USA, mercury-cadmium-telluride detector, 77 K). The potential was applied and the IR spectrum was recorded every 1 min for 10 min. Afterward, the glassy carbon electrode coated with NiCo$_2$O$_4$ sample was retracted from the solution and squeezed the thin layer again for the next potential application. The potential was controlled by the CHI660C electrochemical station in the range of 1.30–1.55 V (vs. RHE). The IR spectrum was collected every 1 min for 10 min

2.7. Operando electrochemical Raman spectroscopy measurement

The active species of HMF selective oxidation to FDCA was identified by operando electrochemical Raman with 532 nm laser, which was performed in a self-made electrochemical Raman cell with thin round quartz glass. The operando electrochemical Raman spectral was tested in a three-electrode configuration. Similarly, NiCo$_2$O$_4$ as the working electrode, Pt wire and Hg/HgO were used as counter electrode and reference electrode, respectively. The Raman spectra of NiCo$_2$O$_4$ electrode were recorded for every minute from 300 to 800 cm^{-1} under different potentials of 1.30–1.55 V (vs. RHE) and different reaction times in HMF-containing KOH electrolyte. The power and exposure time for each spectrum was 50 mW and 10 s, respectively. All Raman spectral peaks were calibrated against the value of 520.5 cm^{-1} of a silicon wafer.

2.8. X-ray absorption fine structure measurement

We tested the Ni and Co K-edge X-Ray Absorption Fine Structure spectra at the BL11B Beamline at Shanghai Synchrotron Radiation Facility (SSRF, Shanghai, China), and all data were tested in fluorescence mode. The X-ray energy was calibrated by stand Ni and Co metal foil. To avoid the influence of the foam nickel substrate, the NiCo$_2$O$_4$ powder samples were ultrasonicated from the Ni foam and coated on carbon paper for testing under different potentials.

3. Results and discussion

3.1. Structural and morphological characterizations of Ni$_x$Co$_{3-x}$O$_4$ electrode

A series of Ni$_x$Co$_{3-x}$O$_4$ crystals with different Co-Co bond lengths near the Ni centers were fabricated via a simple hydrothermal method. The NiO featured a nanosheet structure with 8 nm thickness and it was tightly packed on the Nickel foam (NF) substrate (Fig. S1 a). The Ni$_{1.5}$Co$_{1.5}$O$_4$ and Ni$_2$CoO$_4$ exhibited the composite structures of nanowire and nanosheet (Fig. S1 b–c) with an increased proportion of Co. NiCo$_2$O$_4$ featured an obvious nanowire structure, growing uprightly on the NF substrate (Fig. 1 a–b). Correspondingly, Co$_3$O$_4$ showed an assembled nanowire structure (Fig. S1 d). Ni, Co, and O elements of NiCo$_2$O$_4$ were dispersed uniformly in the nanowires by element mapping (Fig. 1 c–e). The diameter and length of the nanowire were about 42 and 860 nm observed by the TEM, respectively (Fig. 1 f). The HRTEM image (Fig. 1 g) revealed the lattice spacing of 0.24 nm, which was consistent with the (311) plane of NiCo$_2$O$_4$. The crystal structures of the different electrode materials were identified by the XRD spectrum (Fig. 1 h). The diffraction peaks at 18.9°, 31.1°, 36.7°, 44.6°, 59.1°, and 64.9° correspond to the (111), (220), (311), (400), (511), (440) facets of NiCo$_2$O$_4$ (JCPDS:20-0781), respectively [42]. All the Ni$_x$Co$_{3-x}$O$_4$ samples with good stoichemistry are close to those of ideal structures (Fig. 1i).

3.2. HMF oxidation to replace water oxidation for promoting hydrogen production

The effect of the crystal structure of Ni$_x$Co$_{3-x}$O$_4$ crystals on their electrochemical selective oxidation of HMF and simultaneous hydrogen production were explored in a double room H-type cell (Fig. 2 a). Firstly, we evaluated the HMF electrooxidation performance of different electrodes by linear sweep voltammetry (LSV) in 1.0 M KOH with 10 mM HMF. The initial potential of the bare NF electrode and pristine NiO electrode (Fig. 2 b) were very high (>1.30 V vs. RHE), indicating their poor activity. The initial potential decreased obviously such as the Ni$_2$CoO$_4$, Co$_3$O$_4$, Ni$_{1.5}$Co$_{1.5}$O$_4$, NiCo$_2$O$_4$ after the introduction of Co. While neither the Co$_3$O$_4$ nor the Ni$_2$CoO$_4$ performed the lower initial potential. On the contrary, the Ni$_2$CoO$_4$ electrode exhibited a lower initial potential (1.27 V vs. RHE). As mentioned above, different
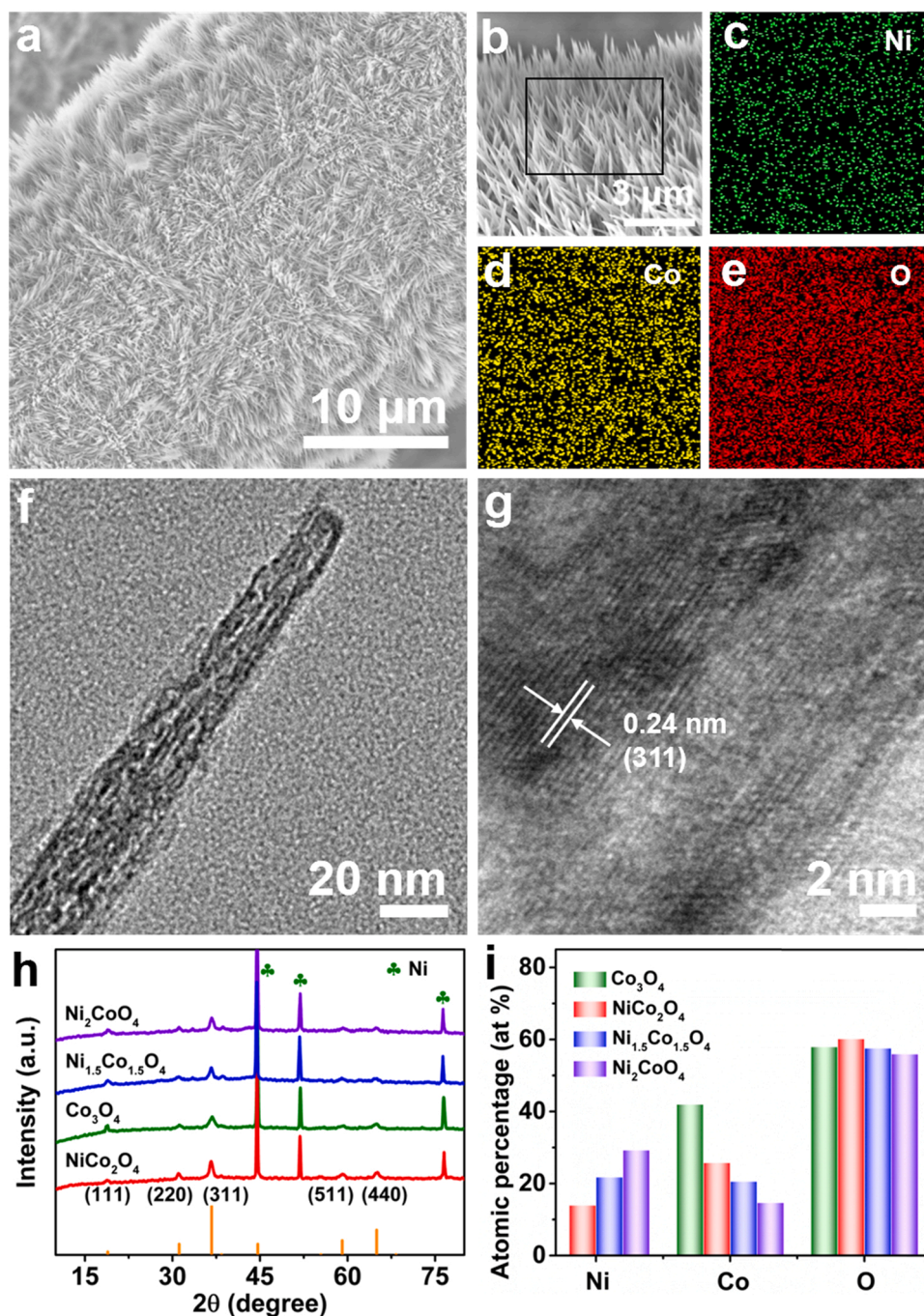
Fig. 1. SEM images (a, b), element mapping of Ni (c) Co (d) O (e), and TEM images (f, g) of $NiCo_2O_4$. XRD (h) and atomic percentage spectrum (i) of different crystal structure electrodes.

electrodes showed different morphology and structures. It can be inferred that the performance difference for HMF electrooxidation of different electrodes may be ascribed to the different specific surface areas. N_2 adsorption-desorption isotherms curve showed that the BET area of $NiCo_2O_4$, $Ni_{1.5}Co_{1.5}O_4$, Co_3O_4, Ni_2CoO_4 and NiO were 134.3, 156.1, 103.7, 198.4 and 79.4 m^2 g^{-1}, respectively (Fig. S2 a–e). Additionally, we have rated the polarization curve normalized by BET area of different electrodes for HMF electrooxidation [46], and the HMF oxidation activity was consistent with geometric area normalized activities: $NiCo_2O_4$ >$Ni_{1.5}Co_{1.5}O_4$ >Co_3O_4 >Ni_2CoO_4 >NiO (Fig. S2 f). The HMF conversions rate constants of NiO, Ni_2CoO_4, Co_3O_4, $Ni_{1.5}Co_{1.5}O_4$, and $NiCo_2O_4$ electrodes were 0.005, 0.009, 0.015, 0.024 and 0.048 min^{-1}, respectively (Figs. 2c S3). The hydrogen production

followed the same order of NiO <Ni_2CoO_4 <Co_3O_4 <$Ni_{1.5}Co_{1.5}O_4$ <$NiCo_2O_4$ (Fig. 2 d). The cathode hydrogen production was positively correlated with anode HMF oxidation. In other words, the hydrogen production was dependent on HMF conversion. The impedance of $NiCo_2O_4$ was lower compared with other electrodes (Fig. S4 a). This might be attributed to the fact that the introduction of Co further improved the kinetics of electron transfer and mass transfer. In short, the $NiCo_2O_4$ anode exhibited the best performance for HMF selective electrooxidation and simultaneous hydrogen production.

Since the oxygen evolution reaction (OER) is the main competitive reaction during the electrocatalytic oxidation of HMF in 1.0 M KOH, so we estimated the onset potential of OER and HMF on the $NiCo_2O_4$ electrode by LSV (Fig. 3 a). In the absence of HMF, the onset potential for
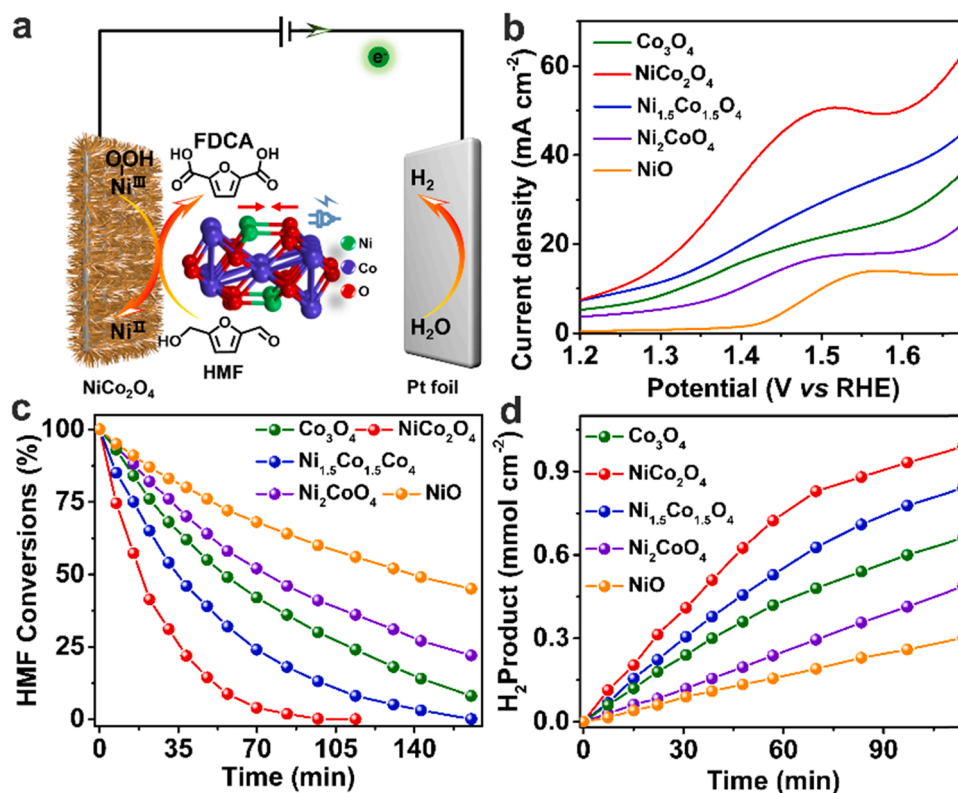
Fig. 2. The schematic diagram of electrochemical HMF oxidation and simultaneous coupled hydrogen production (a). Polarization curves (b), HMF conversions (c), hydrogen production (d) of different crystal structure electrodes.

oxygen evolution is approximately 1.55 V (vs. RHE), and the oxidation peak at 1.38 V (vs. RHE) can be attributed to the oxidation of Ni^{2+}. After the addition of 10 mM HMF in the electrolyte, the current density evidently increased at 1.27 V (vs. RHE), indicating that the oxidation potential of HMF was lower than that of water. More importantly, these intermediate products oxidation of 5-hydroxymethyl-2-furancarboxylic acid (HMFCA), 2,5-diformylfuran (DFF), and 5-formyl-2-furancarboxylic acid (FFCA) were also lower than that of water (Fig. 3 b). It was found that the addition of HMF can reduce the anode overpotential and effectively increase the current density (Fig. S4 b). In the absence of HMF, the potential was 1.68 V (vs. RHE) at the current density of 50 mA cm^{-2}, while after adding 10 mM HMF to the electrolyte, the potential was required to obtain the same current density decreased to 1.47 V (vs. RHE). Similarly, for the current density of 30 mA cm^{-2}, the anode potential decreased from 1.58 V (vs. RHE) to 1.34 V (vs. RHE). It was more promising to replace OER with the thermodynamically more favorable reaction of the HMF oxidation to FDCA to decrease the anode overpotential and simultaneously promote cathode hydrogen production.

The selective conversion of HMF to FDCA was carried out under constant potential to evaluate the HMF conversion yield, FDCA selectivity, and Faradaic efficiency. First, 1.45 V (vs. RHE) was applied for HMF conversion and simultaneous hydrogen production. The HPLC chromatograms of the HMF solution after electrolysis at different reaction stages were recorded (Fig. S4 c c), with 1.25, 1.53, 1.74, and 3.44 min representing the trends of the changes for FDCA, HMFCA, FFCA, and HMF, respectively. It was clearly observed that HMF concentration was reduced with increasing electrolysis time while the concentrations of the generated HMFCA, FFCA, and FDCA were increased. The HMF peak disappeared completely when 190 C charges were passed. The color of the electrolyte was changed to colorless after the electrolysis process (Fig. S5), suggesting the complete conversion of HMF into FDCA. The products were further determined by nuclear

magnetic resonance (NMR). It showed that only HMF was present in the initial stage, while HMFCA and FDCA were also detected after passing 100 C charge, and HMFCA and FDCA were present after 180 C, and only FDCA was detected after 190 C (Fig. S6). Fig. 3 c shows the conversion ratio of HMF and yield of electrochemical oxidation products, it was observed that 99.6% of the HMF was converted into FDCA (yield > 99%), while oxygen was not detected. Thus, a high Faradaic efficiency (>99%) was achieved for the HMF oxidation to FDCA based on the theoretical calculations. In addition, the current density was decreased from the initial value of 45.3–6.4 mA cm^{-2} and finally remained stable with the progress of HMF oxidation (Fig. S4 d). Correspondingly, the hydrogen production rate of the cathode gradually decreased (Fig. 3 d), but the total Faradaic efficiency of hydrogen production still reached 99.1%. The current density in HMF-containing solution (45.3 mA cm^{-2}) was higher than pure water (4.8 mA cm^{-2}) (Fig. S4 d), so that the amount of hydrogen produced in the KOH solution containing HMF was almost 8.16 times higher than that produced using the pure KOH solution (Fig. 3 d). It was also found that the electrons participating in hydrogen production electrons originate mainly from the 6-electron conversion of HMF to FDCA (Fig. 3 e). The selectivity of HMF-to-FDCA and Faradaic efficiency were evaluated under different potentials from 1.35 to 1.60 (vs. RHE) and they were gradually increased with the potential and then decreases (Fig. 3 f).

Meanwhile, we further evaluated the selective conversion of HMF to FDCA under different reaction stages of $Ni_{1.5}Co_{1.5}O_4$, Co_3O_4, Ni_2CoO_4 and NiO electrode system at 1.45 V (vs. RHE) as shown in Fig. 4. It was found that the intermediate product was still mainly HMFCA under different electrodes system. However, the intermediate product of DFF was also detected, especially on the Ni_2CoO_4 and NiO electrodes. After passing the charge of 190 C, the selectivity of FDCA were 97.2%, 95.6%, 92.1% and 88.3% of $Ni_{1.5}Co_{1.5}O_4$, Co_3O_4, Ni_2CoO_4 and NiO electrode, respectively. As the best-in-class electrode in this work, the $NiCo_2O_4$ electrode achieved > 99% selectivity and Faradaic efficiency at 1.45 V
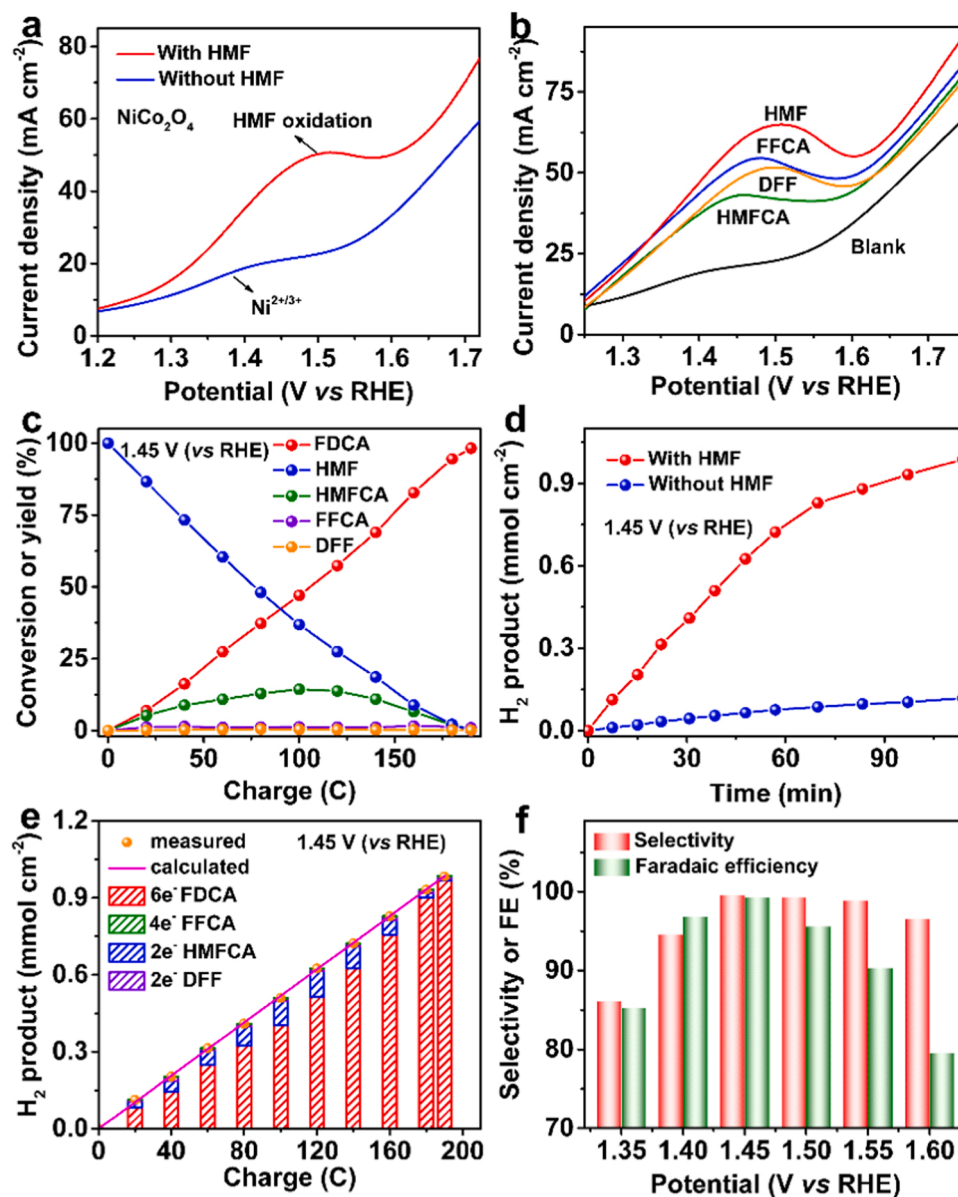
Fig. 3. The polarization curves for the NiCo$_2$O$_4$ electrode in 1 M KOH solution with or without HMF (a) and different substrates (b). HMF conversion (c), hydrogen production (d) and the contribution of different intermediates for hydrogen production (e). The selectivity and Faradaic efficiency of HMF to FDCA under different potentials on NiCo$_2$O$_4$ electrode (f).

(vs. RHE). All these results indicated that the key role of the special crystal structure of Ni$_x$Co$_{3-x}$O$_4$ materials in facilitating the selective electrooxidation of HMF.

Additionally, we evaluated the electrochemical performance of HMF on the NF substrate. The initial potential of NF was high (1.57 V (vs. RHE)), the current density, conversion efficiency (21.3%) of HMF and the amounts of hydrogen production were lower compared with NiCo$_2$O$_4$ electrode (Fig. S7) under 1.45 V (vs. RHE). The result indicated that the impact of NF on HMF conversion can almost be negligible, and NiCo$_2$O$_4$ plays an important role in HMF selective electrooxidation process.

3.3. Mechanism of selective electrooxidation of HMF to FDCA

Indeed, the Co-Co strain in the crystal structure of Ni$_x$Co$_{3-x}$O$_4$ materials could be directly connected with the amounts of as-formed NiOOH during electrochemical reactions and the final activity. The structural model Co$_3$O$_4$, Ni$_2$CoO$_4$, Ni$_{1.5}$Co$_{1.5}$O$_4$ and NiCo$_2$O$_4$ were

shown in Fig. 5 a. Fig. 5 b showed the Co-edge Fourier-transformed (FT) k^3-weighted EXAFS spectra of different crystal structure electrodes, and the peak centered at approximately 1.40 and 2.49 Å were corresponding to the single-scattering path of Co-O and Co-Co of NiCo$_2$O$_4$, respectively. The distances are shorter because the Fourier transform (FT) spectra were not phase-corrected. The Co—Co bond length gradually became shorter, when the content of Co was increased. While not the Co$_3$O$_4$ but the NiCo$_2$O$_4$ exhibited lower bond length and coordination number of Co—Co bond. The fitting result was listed in Table S1 and the wavelet transform also showed the same result (Fig. S8). The Co K-edge EXAFS spectra of Ni$_2$CoO$_4$, Ni$_{1.5}$Co$_{1.5}$O$_4$ and NiCo$_2$O$_4$ indicated the varied Co—Co bond lengths as the main differences between them with fixed Co-Co bond (Figs. 5 b, S8, Table S1), generating different degrees of Co-Co strain accordingly.

High-resolution Ni 2p, Co 2p and O 1 s XPS spectra were obtained to confirm the valence changes of NiCo$_2$O$_4$ before and after the HMF electrooxidation (Fig. 5 c–d). Both Ni^{2+} and Ni^{3+} species only exist in the Ni 2p$_{3/2}$ and Ni 2p$_{1/2}$ spectrum of fresh NiCo$_2$O$_4$ [50–52]. After the
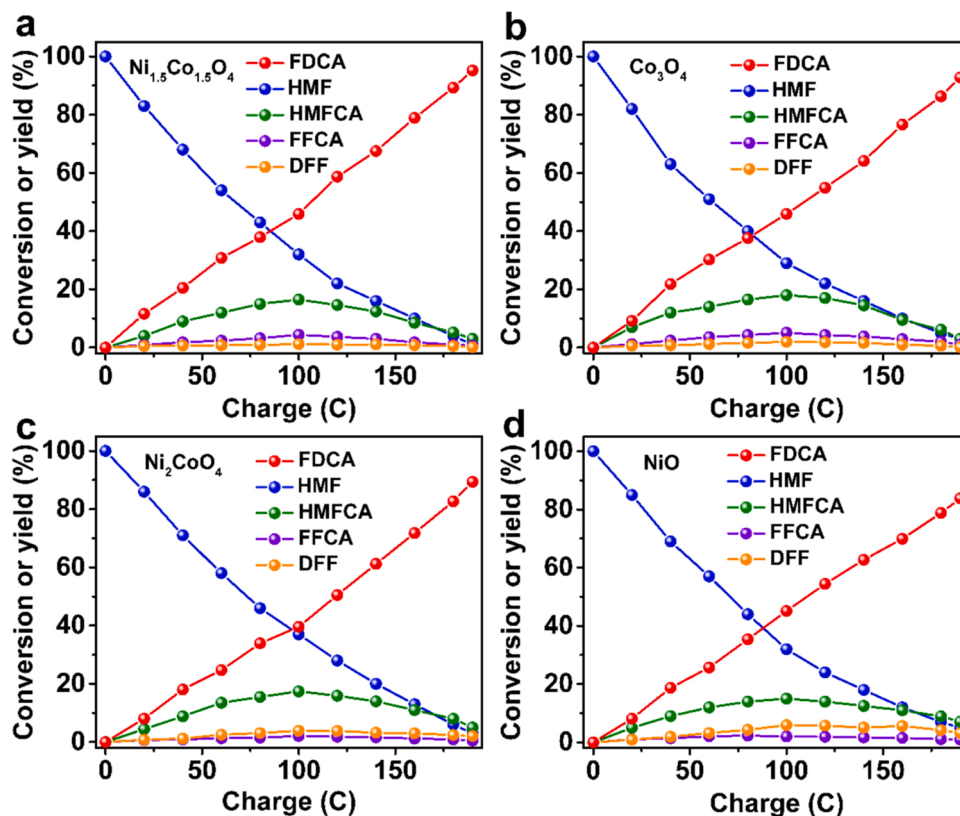
Fig. 4. The conversion rate of HMF and the yield of different products during the electrochemical HMF oxidation at 1.45 V (vs. RHE) under different electrodes (a: $Ni_{1.5}Co_{1.5}O_4$, b: Co_3O_4, c: Ni_2CoO_4, d: NiO).

reaction, the ratio of Ni^{3+}: Ni^{2+} from the fitted Ni 2p XPS spectra increased from 0.70 to 0.89. Meanwhile, the Ni $2p_{3/2}$ binding energy showed a positive shift about 0.4 eV after the electrolysis, suggesting that part of Ni^{2+} was converted into Ni^{3+}, and Ni^{3+} was the major oxide species for the HMF selective conversion (Fig. 5 c). Ni elements became more abundant after the electrolysis in the SEM mapping (Fig. S9 b). By contrast, the Co^{2+} and Co^{3+} species were both present in Co $2p_{3/2}$ and Co $2p_{1/2}$ [53–55], and no obvious differences were observed before and after the reaction (Fig. 5 d) [41]. An examination of the O 1s spectrum showed the presence of three different oxygen species (Fig. S10) with peaks at the binding energies of 529.4, 530.9, and 531.9 eV that are assigned to the metal-oxygen bonds (O1), surface hydroxylated oxygen (O2) and some defect sites with a low oxygen coordination state or chemisorbed water at the $NiCo_2O_4$ surface, respectively. After the reaction, the O1 peak intensity decreased and the O2 band intensity increased, indicating that Ni-O can be further converted into Ni-OOH [47,56]. It can be speculated that Ni^{3+} or higher-valence Ni species can oxidize HMF to FDCA. Specifically, the Co oxidation state can be obtained from the Co K-edge energy shift and it was approximately + 2.67 (Fig. S11 a–b). Interestingly, the absorption position of the Co K-edge was not clearly shifted by applying potential from 1.40 to 1.60 V (vs. RHE) [57], indicating that Co remained as the mixture of Co (II) and Co (III) and the valence did not change significantly during the HMF electrochemical oxidation process (Fig. S11c–d). The result was consistent with the Co 2p XPS (Fig. 5 d). The changes almost can be ignored in the Co K-edge EXAFS of $NiCo_2O_4$, which indicated the potential will not affect the strain of Co-Co (Fig. 5 e). The SEM mapping showed that the content of Co has not changed significantly after the reaction of electrochemical oxidation of HMF (Fig. S9 c). Meanwhile, it was found that the peak intensity of the Co-Ni path was increased in the Co K-edge EXAFS spectra after applying the potential. The main reason is that the application of potential increases the coordination number, improves symmetry, and reduces the disorder of the Co-Ni bond. The fitting result

of Co K-edge of $NiCo_2O_4$ before and after electrochemical HMF oxidation was listed in Table S2 and the changes can also be ignored. The Ni average valence state of $NiCo_2O_4$ was estimated as + 2.23 (Fig. S11 e–f). This may be due to either further orbital hybridization between the Ni 3d and O 2p orbitals, or electron transfer from the Ni 3d to the Co 3d orbital [58]. The pre-edge peak at the Ni K-edge indicated that the Ni is distributed at the octahedral sites [59,60]. However, the Ni K-edge X-ray absorption near-edge structure (XANES) spectrum showed the absorption edge energy gradually increases with the potential varied from 1.40 to 1.60 V (vs. RHE) (Fig. S11 g–h), which indicated that the Ni valence state gradually increased with potential. This result was consistent with the Ni 2p XPS results (Fig. 5 c). Meanwhile, the white line intensity of the Ni K-edge XANES spectra exhibited a considerable decrease when the applied potential was increased, indicating that $NiCo_2O_4$ evolved into a distorted octahedral structure during the oxidation process. More importantly, the autoxidation of Ni^{2+} to Ni^{3+}, mainly in the form of NiOOH as already demonstrated in previous work [61–64], could proceed in all $Ni_xCo_{3-x}O_4$ samples during the electrochemical reactions with the oxidation state and bond lengths of Co components unchanged, indicating the role of Co—Co bond as a stable host for anchoring the Ni species.

The in situ formed NiOOH active species for HMF selective oxidation under 1.45 V (vs. RHE) at different degrees of Co-Co strain crystal structure was further identified by operando electrochemical Raman technology. The operando electrochemical Raman analysis (Fig. 5 f) results further demonstrated the in situ formed NiOOH with typical peaks centered at 474 and 554 cm^{-1} in all $Ni_xCo_{3-x}O_4$ samples [40,61, 65–67]. More importantly, the amounts of as-formed NiOOH species as indicated by the Raman peak relative intensities under fixed conditions match well with the trend of varied Co—Co bond strain in $Ni_xCo_{3-x}O_4$ crystals (Fig. 5 b). As the enhanced strain of the Co—Co bond, more NiOOH species formed during the reaction process accelerate the conversions of HMF (Fig. 5 g), accordingly. As a result, the $NiCo_2O_4$ sample
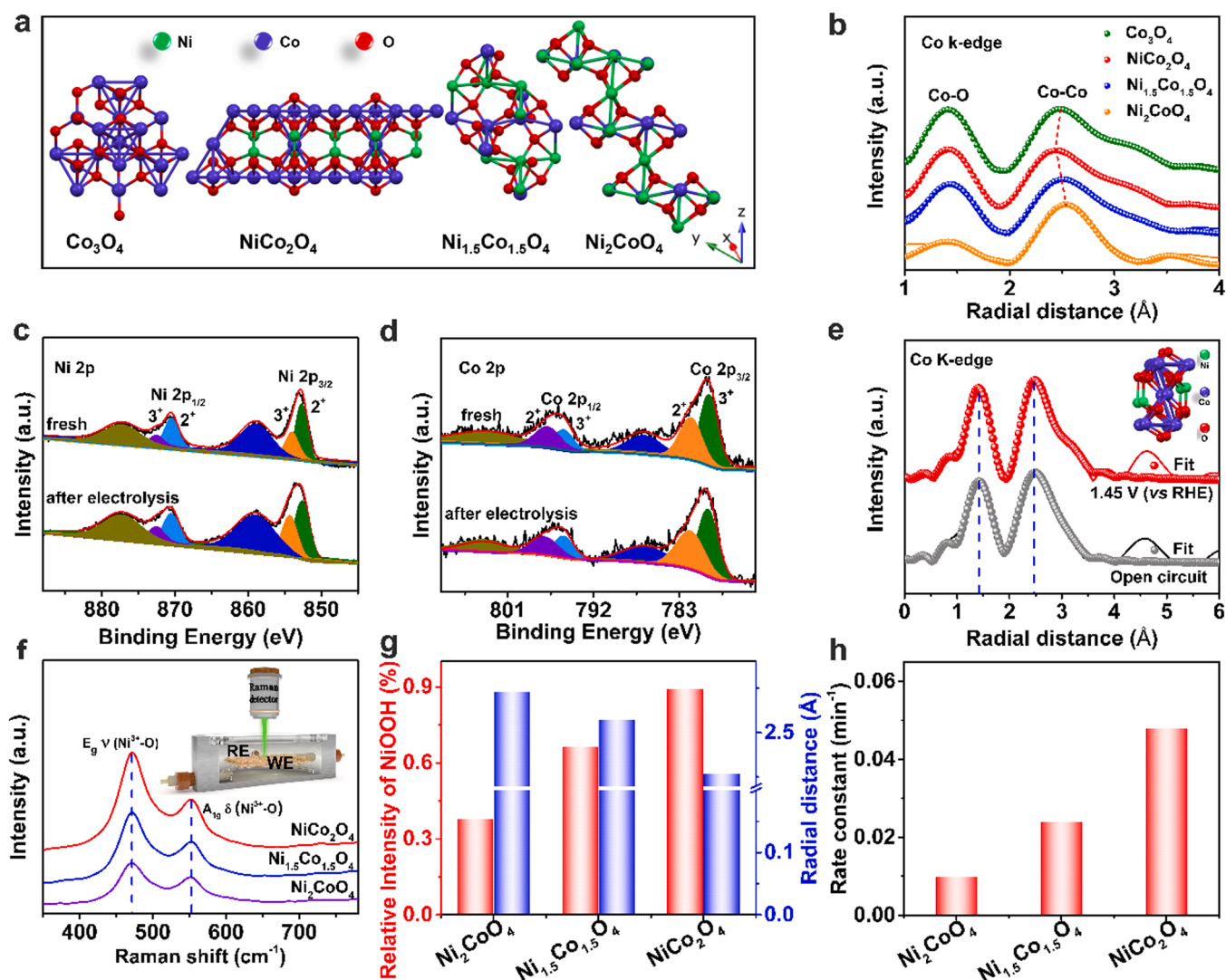
Fig. 5. The structural model (a) and EXAFS spectra (b) of Co K-edge of different crystal structure electrodes. High-resolution XPS spectra of Ni 2p (c), Co 2p (d), and the Co K-edge EXAFS spectra (e) of $NiCo_2O_4$ before and after the HMF electrooxidation. Operando Raman spectra of different crystal structure electrodes (f), and the insert image of Operando electrochemistry Raman experimental setup diagram (WE, working electrode; CE, counter electrode; RE, reference electrode). The relationship between the formation of NiOOH and the strain of Co—Co bond (g), rate constant of HMF conversion (h) of different crystal structure electrodes.

with the heaviest Co-Co strain gives rise to form the highest amount of NiOOH active center compared with other electrodes system (Fig. 5 g), well explaining their excellent performance for electrochemical HMF conversion (Fig. 5 h).

We used $NiCo_2O_4$ as the optimal sample to further verify the electrochemical formation mechanism of NiOOH during the electrochemical HMF oxidation process. Although the Co—Co bonds could be maintained well during the reaction process, the Co-Co strain can make the Ni species very sensitive to the applied voltage. Fig. 6 **a** showed the wavelet transform of $NiCo_2O_4$ under different potentials. Two intensity maxima at approximately 1.46 and 2.48 Å that were ascribed to the Ni-O and Ni—Ni bond were observed under an open circuit. Similarly, the fitting results were in good agreement with the $NiCo_2O_4$ model without the applied potential. The high-density distribution area of the Ni—O bond was reduced from 2 to 3–1–2 as the potential increased. The wavelet transform images of $NiCo_2O_4$ estimated from the operando EXAFS analysis results (Fig. 6 a and Table S3) directly reveal gradually shortened Ni-O bonds (Fig. 6 a–b) under ever elevated working voltage. It must be noted that the fitting result was consistent with the model of NiOOH. Accordingly, the gradually decreased coordination numbers of Ni-O bond in the $NiCo_2O_4$ electrode via from 6.42 to 4.74 (Table S3) at a

potential of an open circuit to 1.50 V (vs. RHE), respectively, directly indicate the in situ oxidation of Ni into NiOOH species. The more NiOOH is formed in situ with increased potential and time in the HMF-containing KOH electrolyte identified by operando Raman technology (Figs. 6 c, S12). The result indicated that the sensitivity of the Ni—O bond to voltage can be regulated by the Co—Co bond strain of the crystal structure to induce the formation of more NiOOH active species in the $NiCo_2O_4$ material. Additionally, the Raman signals of the $NiCo_2O_4$ electrode were collected under different potentials in a pure KOH solution, and the peak intensity of 474 cm^{-1} and 554 cm^{-1} was higher than the HMF-containing KOH solution. When we disconnected the circuit and added HMF to the pure KOH solution, it was found that the two peaks gradually weakened with increasing time and disappeared after approximately 120 s. The reason was that HMF acts as a quencher for Ni^{3+} oxidation. It was concluded that Ni (III)-OOH was formed on the $NiCo_2O_4$ surface in the HMF solution first, and then quickly oxidized HMF to FDCA. Meanwhile, Ni (III) was reduced to Ni (II), so that the peaks of NiOOH observed from the operando Raman spectra were lower than pure KOH electrolyte (Fig. S12). Though, some literature has also reported that the Raman characteristic peak of A_{1g} and E_g vibrational modes of Co-O bond in CoOOH species was located at 508 and 608 cm^{-1}
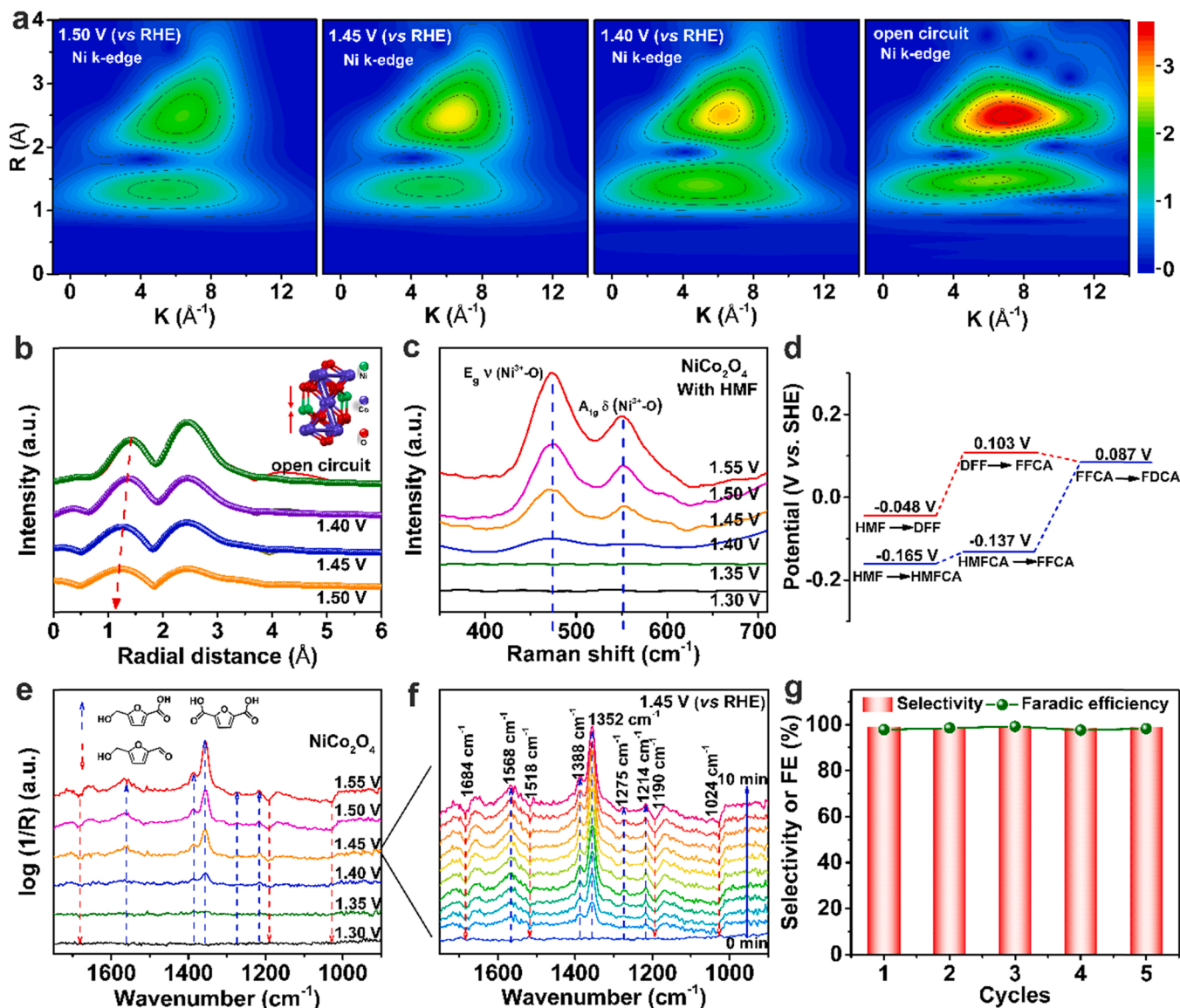
Fig. 6. The wavelet transformation (a) and the corresponding EXAFS fitting curves (b) of the Ni K-edge of $NiCo_2O_4$ electrode under different potential. Operando electrochemical Raman of $NiCo_2O_4$ electrode under different potentials in the HMF-containing KOH solution (c). DFT calculation of the oxidation potential of different reaction paths for HMF to FDCA (d).Operando EC-IR spectrum of $NiCo_2O_4$ electrode for HMF electrooxidation under different potential and times (e, f). The selectivity and Faradaic efficiencies of HMF to FDCA under $NiCo_2O_4$ electrode at 1.45 V (vs. RHE) for five successive cycles (g).

[68–75]. In the Raman spectra of different electrodes and $NiCo_2O_4$ electrode for HMF electrooxidation under different potentials, the characteristic peak of CoOOH was not observed, especially the overlapping area of 508 cm^{-1}.

It was apparent that a stronger change was observed for the Ni cations than for the Co cations, indicating that Ni cations play an important role in HMF oxidation. However, the role of Co cations of $NiCo_2O_4$ cannot be totally ignored during HMF oxidation, because the greater activity of Ni cation may arise due to the coordinated Co cations and oxygen anions. Meanwhile, it was also reported that Co oxide can also act as a scaffold to provide a conductive matrix for the charge carriers [65]. The electronic configuration of Ni^{2+} is $t_{2g}^6 e_g^2$, while that of Ni^{3+} is $t_{2g}^6 e_g^1$, with a near-unity occupancy of the e_g orbital. It was known that the higher the orbital occupancy of surface metal ions, the more covalent bond of metal-oxygen can be increased, and it is considered as the optimal electron configuration for the adsorption/desorption of oxygen-containing reaction. It can be speculated that Ni facilitates the adsorption of HMF on the electrode surface, with NiOOH as the

dominant active site for the HMF electrochemical oxidation, while Co mainly promotes the formation of NiOOH [42].

The strain-induced in situ formation of NiOOH can further regulate the reaction pathway of HMF to FDCA. Two possible conversion pathways were presented due to the coexistence of -CHO and -OH on HMF (Fig. S13). It was reported that the aldehyde groups preferentially adsorbed on the catalyst surface than hydroxyl groups in a strongly alkaline environment, so that the aldehyde was firstly oxidized to form HMFCA in Ni-based materials [26,40,76–78]. Then, we further modeled the standard potential of the HMF oxidation to FDCA by density functional theory (DFT) calculations as shown in Fig. 6 d. It was clearly observed that the standard potential of HMF to HMFCA was −0.165 V (vs SHE), which was lower than HMF to DFF (−0.048 V), so that HMFCA was considered as the optimal intermediate for HMF to FDCA conversion [45,56]. The potential of Ni^{3+}/Ni^{2+} was about 0.49 V (vs SHE), which could be expected to drive each step during the oxidation of HMF to FDCA.

Besides, we design an operando electrochemical infrared thin-layer device to further identify the HMF conversion path on the $NiCo_2O_4$

electrode surface (Fig. S14). The downward peaks at 1024, 1190, 1518 and 1684 cm^{-1} represent the consumption of HMF. The upward peaks at 1352, 1388, and 1568 cm^{-1} represent the formation of HMFCA. The peaks of 1275 and 1405 cm^{-1} were attributed to FFCA [79,80]. The bands at 1352 cm^{-1} can be ascribed to the carboxyl group symmetrical stretching vibration of FDCA or FFCA. The change at 1388 cm^{-1} can be attributed to the formation of FDCA. The detailed attribution of different vibration peaks was shown in Table S4. No peak was observed at 1.30 and 1.35 V (vs RHE). These peak intensity at 1190 and 1024 cm^{-1} gradually decreased and the peaks at 1352, 1388 and 1568 cm^{-1} were significantly enhanced as the potential and time increased, indicating the consumption of HMF and the formation of HMFCA and FDCA (Figs. 6 e–f, S15). The operando EC-IR confirmed that the path of HMF conversion to FDCA proceed through HMFCA, which was in accordance with the HPLC and NMR results. It has been demonstrated that the strain-induced in situ formation NiOOH species is more conducive to oxidizing -CHO, not -OH, when the -OH and -CHO coexistence.

The cycle test of HMF conversion and simultaneous hydrogen production were performed five times at 1.45 V (vs. RHE) under the NiCo$_2$O$_4$ electrode. After adding HMF many times, the current density can still reach the initial state (Fig. S16). NiCo$_2$O$_4$ electrode with the shortest Co—Co bonds still showed excellent performance for HMF conversion (>99% selectivity and Faradaic efficiency) and simultaneous hydrogen production (0.986 mmol cm^{-2} Figs. 6 g, S17). After the reaction, the NiCo$_2$O$_4$ electrode morphology was not changed significantly, and the NiCo$_2$O$_4$ nanowire was still tightly loaded on the nickel foam substrate without quality loss (Fig. S9 a). The SEM-Mapping of fresh and after electrolysis of NiCo$_2$O$_4$ electrode showed that the Ni, Co and O elements were still evenly distributed on the nickel foam substrate. All these results indicated that an unchanged Co—Co bond can maintain the stability of the structure, while the changed Ni-O bond can further induce more NiOOH formation in situ to improve catalytic activity and stability simultaneously.

4. Conclusion

In summary, a series of Ni$_x$Co$_{3-x}$O$_4$ electrodes were prepared by a simple hydrothermal method. The selective conversion of HMF to FDCA (selectivity and Faradaic efficiency, >99%) was achieved at 1.45 V (vs. RHE) and the amounts of hydrogen production are 8.16 times higher than that for pure water, indicating that the selective conversion of HMF to FDCA can replace water oxidation to achieve a significant enhancement of hydrogen production. Additionally, we identified the formation mechanism of NiOOH species, the most effective catalyst for selective electrooxidation of HMF to FDCA. We developed operando characterization systems using EXAFS, DFT, FTIR and Raman to demonstrate the crystal-strain induced formation of NiOOH from Ni-O induced by the Co—Co bond strain and such a crystal strain could be further enhanced by the electric field for the in situ formation of more NiOOH species. The HMF conversion rate depends on the content of in situ formed NiOOH instead of Ni in the material. NMR, DFT and operando EC-IR identified that the reaction path was HMF-HMFCA-FFCA-FDCA. In general, this work further reveals the in situ formation mechanism of NiOOH in transition metal-based catalysts, and provides insights to design efficient electrocatalysts for the selective conversion of other biomass derivatives.

CRediT authorship contribution statement

Zhaoyu Zhou: Conceptualization, Formal analysis, Methodology, Investigation, Data curation, Writing – original draft, Writing – review & editing. **Ya-nan Xie:** Conceptualization, Validation, Formal analysis, Investigation. **Lingzhi Sun:** Methodology, Investigation. **Zhiming Wang:** Methodology, Investigation. **Weikang Wang:** Methodology, Investigation. **Luozhen Jiang:** Resources, Validation. **Xin Tao:** Resources, Validation. **Lina Li:** Resources, Validation, Investigation. **Xin-**

Hao Li: Conceptualization, Writing – original draft, Validation. **Guohua Zhao:** Supervision, Conceptualization, Funding acquisition.

Declaration of Competing Interest

The authors declare that they have no known competing financial interests or personal relationships that could have appeared to influence the work reported in this paper.

Acknowledgements

Appendix A. Supporting information

Supplementary data associated with this article can be found in the online version at doi:10.1016/j.apcatb.2022.121072.

References

[1] C. Tang, Y. Zheng, M. Jaroniec, S.-Z. Qiao, Electrocatalytic refinery for sustainable production of fuels and chemicals, Angew. Chem. Int. Ed. 60 (2021) 19572–19590, https://doi.org/10.1002/anie.202101522.

[2] X. Wu, N. Luo, S. Xie, H. Zhang, Q. Zhang, F. Wang, Y. Wang, Photocatalytic transformations of lignocellulosic biomass into chemicals, Chem. Soc. Rev. 49 (2020) 6198–6223, https://doi.org/10.1039/d0cs00314j.

[3] Y. Li, X. Wei, L. Chen, J. Shi, Electrocatalytic hydrogen production trilogy, Angew. Chem. Int. Ed. 60 (2021) 19550–19571, https://doi.org/10.1002/anie.202009854.

[4] F. Valentini, V. Kozell, C. Petrucci, A. Marrocchi, Y. Gu, D. Gelman, L. Vaccaro, Formic acid, a biomass-derived source of energy and hydrogen for biomass upgrading, Energy Environ. Sci. 12 (2019) 2646–2664, https://doi.org/10.1039/c9ee01747j.

[5] J. Byun, J. Han, Sustainable development of biorefineries: integrated assessment method for co-production pathways, Energy Environ. Sci. 13 (2020) 2233–2242, https://doi.org/10.1039/d0ee00812e.

[6] S. Albonetti, A. Lolli, V. Morandi, A. Migliori, C. Lucarelli, F. Cavani, Conversion of 5-hydroxymethylfurfural to 2,5-furandicarboxylic acid over Au-based catalysts: optimization of active phase and metal–support interaction, Appl. Catal. B Environ. 163 (2015) 520–530, https://doi.org/10.1016/j.apcatb.2014.08.026.

[7] K. Gupta, R.K. Rai, S.K. Singh, Metal catalysts for the efficient transformation of biomass-derived HMF and furfural to value added chemicals, ChemCatChem 10 (2018) 2326–2349, https://doi.org/10.1002/cctc.201701754.

[8] H.-F. Ye, R. Shi, X. Yang, W.-F. Fu, Y. Chen, P-doped ZnxCd1-xS solid solutions as photocatalysts for hydrogen evolution from water splitting coupled with photocatalytic oxidation of 5-hydroxymethylfurfural, Appl. Catal. B Environ. 233 (2018) 70–79, https://doi.org/10.1016/j.apcatb.2018.03.060.

[9] M. Sajid, X. Zhao, D. Liu, Production of 2,5-furandicarboxylic acid (FDCA) from 5-hydroxymethylfurfural (HMF): recent progress focusing on the chemical-catalytic routes, Green Chem. 20 (2018) 5427–5453, https://doi.org/10.1039/c8gc02680g.

[10] B. Zhu, C. Chen, L. Huai, Z. Zhou, L. Wang, J. Zhang, 2,5-Bis(hydroxymethyl)furan: A new alternative to HMF for simultaneously electrocatalytic production of FDCA and H$_2$ over CoOOH/Ni electrodes, Appl. Catal. B Environ. 297 (2021), 120396, https://doi.org/10.1016/j.apcatb.2021.120396.

[11] Z. Zhou, C. Chen, M. Gao, B. Xia, J. Zhang, In situ anchoring of a Co$_3$O$_4$ nanowire on nickel foam: an outstanding bifunctional catalyst for energy-saving simultaneous reactions, Green Chem. 21 (2019) 6699–6706, https://doi.org/10.1039/c9gc02880c.

[12] H.G. Cha, K.S. Choi, Combined biomass valorization and hydrogen production in a photoelectrochemical cell, Nat. Chem. 7 (2015) 328–333, https://doi.org/10.1038/nchem.2194.

[13] Z. Gao, G. Fan, M. Liu, L. Yang, F. Li, Dandelion-like cobalt oxide microsphere-supported RuCo bimetallic catalyst for highly efficient hydrogenolysis of 5-hydroxymethylfurfural, Appl. Catal. B Environ. 237 (2018) 649–659, https://doi.org/10.1016/j.apcatb.2018.06.026.

[14] B. Yang, W. Hu, F. Wan, C. Zhang, Z. Fu, A. Su, M. Chen, Y. Liu, Adjusting effect of additives on decatungstate-photocatalyzed HMF oxidation with molecular oxygen under visible light illumination, Chem. Eng. J. 396 (2020), 125345, https://doi.org/10.1016/j.cej.2020.125345.

[15] W.-J. Liu, L. Dang, Z. Xu, H.-Q. Yu, S. Jin, G.W. Huber, Electrochemical oxidation of 5-hydroxymethylfurfural with NiFe layered double hydroxide (LDH) nanosheet catalysts, ACS Catal. 8 (2018) 5533–5541, https://doi.org/10.1021/acscatal.8b01017.

[16] Y.-T. Liao, C. Nguyen Van, N. Ishiguro, A.P. Young, C.-K. Tsung, K.C.W. Wu, Engineering a homogeneous alloy-oxide interface derived from metal-organic frameworks for selective oxidation of 5-hydroxymethylfurfural to 2, 5-furandicarboxylic acid, Appl. Catal. B Environ. 270 (2020), 118805, https://doi.org/10.1016/j.apcatb.2020.118805.

[17] D.-H. Nam, B.J. Taitt, K.-S. Choi, Copper-based catalytic anodes to produce 2,5-furandicarboxylic acid, a biomass-derived alternative to terephthalic acid, ACS Catal. 8 (2018) 1197–1206, https://doi.org/10.1021/acscatal.7b03152.

[18] A. Tirsoaga, M. El Fergani, N. Nuns, P. Simon, P. Granger, V.I. Parvulescu, S. M. Coman, Multifunctional nanocomposites with non-precious metals and magnetic core for 5-HMF oxidation to FDCA, Appl. Catal. B Environ. 278 (2020), 119309, https://doi.org/10.1016/j.apcatb.2020.119309.

[19] B.J. Taitt, D.-H. Nam, K.-S. Choi, A comparative study of nickel, cobalt, and iron oxyhydroxide anodes for the electrochemical oxidation of 5-hydroxymethylfurfural to 2,5-furandicarboxylic acid, ACS Catal. 9 (2018) 660–670, https://doi.org/10.1021/acscatal.8b04003.

[20] S. Liang, L. Pan, T. Thomas, B. Zhu, C. Chen, J. Zhang, H. Shen, J. Liu, M. Yang, Ni3N-V2O3 enables highly efficient 5-(Hydroxymethyl) furfural oxidation enabling membrane free hydrogen production, Chem. Eng. J. 415 (2021), 128864, https://doi.org/10.1016/j.cej.2021.128864.

[21] F. Neațu, R.S. Marin, M. Florea, N. Petrea, O.D. Pavel, V.I. Pârvulescu, Selective oxidation of 5-hydroxymethyl furfural over non-precious metal heterogeneous catalysts, Appl. Catal. B Environ. 180 (2016) 751–757, https://doi.org/10.1016/j.apcatb.2015.07.043.

[22] K.T.V. Rao, Y. Hu, Z. Yuan, Y. Zhang, C. Xu, Nitrogen-doped carbon: a metal-free catalyst for selective oxidation of crude 5-hydroxymethylfurfural obtained from high fructose corn syrup (HFCS-90) to 2,5-furandicarboxylic acid (FDCA), Chem. Eng. J. 404 (2021), 127063, https://doi.org/10.1016/j.cej.2020.127063.

[23] X. Deng, M. Li, Y. Fan, L. Wang, X.-Z. Fu, J.-L. Luo, Constructing multifunctional 'Nanoplatelet-on-Nanoarray' electrocatalyst with unprecedented activity towards novel selective organic oxidation reactions to boost hydrogen production, Appl. Catal. B Environ. 278 (2020), 119339, https://doi.org/10.1016/j.apcatb.2020.119339.

[24] C. Yang, C. Wang, L. Zhou, W. Duan, Y. Song, F. Zhang, Y. Zhen, J. Zhang, W. Bao, Y. Lu, D. Wang, F. Fu, Refining d-band center in Ni0.85Se by Mo doping: a strategy for boosting hydrogen generation via coupling electrocatalytic oxidation 5-hydroxymethylfurfural, Chem. Eng. J. 422 (2021) 130125, https://doi.org/10.1016/j.cej.2021.130125.

[25] R.S. Assary, P.C. Redfern, J.R. Hammond, J. Greeley, L.A. Curtiss, Predicted thermochemistry for chemical conversions of 5-hydroxymethylfurfural, Chem. Phys. Lett. 497 (2010) 123–128, https://doi.org/10.1016/j.cplett.2010.07.082.

[26] Y. Yang, T. Mu, Electrochemical oxidation of biomass derived 5-hydroxymethyl-furfural (HMF): pathway, mechanism, catalysts and coupling reactions, Green Chem. 23 (2021) 4228–4254, https://doi.org/10.1039/d1gc00914a.

[27] O.R. Schade, K.F. Kalz, D. Neukum, W. Kleist, J.-D. Grunwaldt, Supported gold- and silver-based catalysts for the selective aerobic oxidation of 5-(hydroxymethyl) furfural to 2,5-furandicarboxylic acid and 5-hydroxymethyl-2-furancarboxylic acid, Green Chem. 20 (2018) 3530–3541, https://doi.org/10.1039/c8gc01340c.

[28] G. Yang, Y. Jiao, H. Yan, Y. Xie, A. Wu, X. Dong, D. Guo, C. Tian, H. Fu, Interfacial engineering of MoO2-FeP heterojunction for highly efficient hydrogen evolution coupled with biomass electrooxidation, Adv. Mater. 32 (2020), 2000455, https://doi.org/10.1002/adma.202000455.

[29] D.J. Chadderdon, L. Xin, J. Qi, Y. Qiu, P. Krishna, K.L. More, W. Li, Electrocatalytic oxidation of 5-hydroxymethylfurfural to 2,5-furandicarboxylic acid on supported Au and Pd bimetallic nanoparticles, Green Chem. 16 (2014) 3778–3786, https://doi.org/10.1039/c4gc00401a.

[30] B. You, N. Jiang, X. Liu, Y. Sun, Simultaneous H2 generation and biomass upgrading in water by an efficient noble-metal-free bifunctional electrocatalyst, Angew. Chem. Int. Ed. 55 (2016) 9913–9917, https://doi.org/10.1002/anie.201603798.

[31] N. Jiang, B. You, R. Boonstra, I.M. Terrero Rodriguez, Y. Sun, Integrating electrocatalytic 5-hydroxymethylfurfural oxidation and hydrogen production via Co-P-derived electrocatalysts, ACS Energy Lett. 1 (2016) 386–390, https://doi.org/10.1021/acsenergylett.6b00214.

[32] M.J. Kang, H. Park, J. Jegal, S.Y. Hwang, Y.S. Kang, H.G. Cha, Electrocatalysis of 5-hydroxymethylfurfural at cobalt based spinel catalysts with filamentous nanoarchitecture in alkaline media, Appl. Catal. B Environ. 242 (2019) 85–91, https://doi.org/10.1016/j.apcatb.2018.09.087.

[33] B. You, X. Liu, N. Jiang, Y. Sun, A general strategy for decoupled hydrogen production from water splitting by integrating oxidative biomass valorization, J. Am. Chem. Soc. 138 (2016) 13639–13646, https://doi.org/10.1021/jacs.6b07127.

[34] G. Han, Y.-H. Jin, R.A. Burgess, N.E. Dickenson, X.M. Cao, Y. Sun, Visible-light-driven valorization of biomass intermediates integrated with H2 production catalyzed by ultrathin Ni/CdS nanosheets, J. Am. Chem. Soc. 139 (2017) 15584–15587, https://doi.org/10.1021/jacs.7b08657.

[35] X. Lu, K.-H. Wu, B. Zhang, J. Chen, F. Li, B.-J. Su, P. Yan, J.-M. Chen, W. Qi, Highly efficient electro-reforming of 5-hydroxymethylfurfural on vertically oriented nickel nanosheet/carbon hybrid catalysts: structure-function relationships, Angew. Chem. Int. Ed. 60 (2021) 14528–14535, https://doi.org/10.1002/anie.202102359.

[36] S. De, J. Zhang, R. Luque, N. Yan, Ni-based bimetallic heterogeneous catalysts for energy and environmental applications, Energy Environ. Sci. 9 (2016) 3314–3347, https://doi.org/10.1039/c6ee02002j.

[37] F. Kong, M. Wang, Preparation of sulfur-modulated nickel/carbon composites from lignosulfonate for the electrocatalytic oxidation of 5-hydroxymethylfurfural to 2,5-furandicarboxylic acid, ACS Appl. Energy Mater. 4 (2021) 1182–1188, https://doi.org/10.1021/acsaem.0c02418.

[38] W. Wang, F. Kong, Z. Zhang, L. Yang, M. Wang, Sulfidation of nickel foam with enhanced electrocatalytic oxidation of 5-hydroxymethylfurfural to 2,5-furandi-carboxylic acid, Dalton Trans. 50 (2021) 10922–10927, https://doi.org/10.1039/d1dt02025k.

[39] K. Gu, D. Wang, C. Xie, T. Wang, G. Huang, Y. Liu, Y. Zou, L. Tao, S. Wang, Defect-rich high-entropy oxide nanosheets for efficient 5-hydroxymethylfurfural electrooxidation, Angew. Chem. Int. Ed. 60 (2021) 20253–20258, https://doi.org/10.1002/anie.202107390.

[40] N. Heidary, N. Kornienko, Electrochemical biomass valorization on gold-metal oxide nanoscale heterojunctions enables investigation of both catalyst and reaction dynamics with operando surface-enhanced Raman spectroscopy, Chem. Sci. 11 (2020) 1798–1806, https://doi.org/10.1039/d0sc00136h.

[41] Y. Lu, C.-L. Dong, Y.-C. Huang, Y. Zou, Y. Liu, Y. Li, N. Zhang, W. Chen, L. Zhou, H. Lin, S. Wang, Hierarchically nanostructured NiO-Co3O4 with rich interface defects for the electro-oxidation of 5-hydroxymethylfurfural, Sci. China Chem. 63 (2020) 980–986, https://doi.org/10.1007/s11426-020-9749-8.

[42] H. Wang, C. Li, J. An, Y. Zhuang, S. Tao, Surface reconstruction of NiCoP for enhanced biomass upgrading, J. Mater. Chem. A 9 (2021) 18421–18430, https://doi.org/10.1039/d1ta05425b.

[43] R. Latsuzbaia, R. Bisselink, A. Anastasopol, H. van der Meer, R. van Heck, M. S. Yagüe, M. Zijlstra, M. Roelands, M. Crockatt, E. Goetheer, E. Giling, Continuous electrochemical oxidation of biomass derived 5-(hydroxymethyl)furfural into 2,5-furandicarboxylic acid, J. Appl. Electrochem. 48 (2018) 611–626, https://doi.org/10.1007/s10800-018-1157-7.

[44] N. Zhang, Y. Zou, L. Tao, W. Chen, L. Zhou, Z. Liu, B. Zhou, G. Huang, H. Lin, S. Wang, Electrochemical oxidation of 5-hydroxymethylfurfural on nickel nitride/carbon nanosheets: reaction pathway determined by in situ sum frequency generation vibrational spectroscopy, Angew. Chem. Int. Ed. 58 (2019) 15895–15903, https://doi.org/10.1002/anie.201908722.

[45] P. Zhang, X. Sheng, X. Chen, Z. Fang, J. Jiang, M. Wang, F. Li, L. Fan, Y. Ren, B. Zhang, B.J.J. Timmer, M.S.G. Ahlquist, L. Sun, Paired electrocatalytic oxygenation and hydrogenation of organic substrates with water as the oxygen and hydrogen source, Angew. Chem. Int Ed. Engl. 58 (2019) 9155–9159, https://doi.org/10.1002/anie.201903936.

[46] Y. Lu, C.-L. Dong, Y.-C. Huang, Y. Zou, Z. Liu, Y. Liu, Y. Li, N. He, J. Shi, S. Wang, Identifying the geometric site dependence of spinel oxides for the electrooxidation of 5-hydroxymethylfurfural, Angew. Chem. Int. Ed. 59 (2020) 19215–19221, https://doi.org/10.1002/anie.202007767.

[47] L. Gao, Y. Bao, S. Gan, Z. Sun, Z. Song, D. Han, F. Li, L. Niu, Hierarchical nickel-cobalt-based transition metal oxide catalysts for the electrochemical conversion of biomass into valuable chemicals, ChemSusChem 11 (2018) 2547–2553, https://doi.org/10.1002/cssc.201800695.

[48] Z. Zhou, L. Zeng, G. Xiong, L. Yang, H. Yuan, J. Yu, S. Xu, D. Wang, X. Zhang, H. Liu, W. Zhou, Multifunctional electrocatalyst of NiCo-NiCoP nanoparticles embedded into P-doped carbon nanotubes for Energy-Saving hydrogen production and upgraded conversion of formaldehyde, Chem. Eng. J. 426 (2021), 129214, https://doi.org/10.1016/j.cej.2021.129214.

[49] P.V. Rathod, V.H. Jadhav, Efficient method for synthesis of 2,5-furandicarboxylic acid from 5-hydroxymethylfurfural and fructose using Pd/CC catalyst under aqueous conditions, ACS Sustain. Chem. Eng. 6 (2018) 5766–5771, https://doi.org/10.1021/acssuschemeng.7b03124.

[50] K. Guo, Y. Wang, J. Huang, M. Lu, H. Li, Y. Peng, P. Xi, H. Zhang, J. Huang, S. Lu, C. Xu, In situ activated Co3–xNixO4 as a highly active and ultrastable electrocatalyst for hydrogen generation, ACS Catal. 11 (2021) 8174–8182, https://doi.org/10.1021/acscatal.1c01607.

[51] H. Yuan, J. Li, W. Yang, Z. Zhuang, Y. Zhao, L. He, L. Xu, X. Liao, R. Zhu, L. Mai, Oxygen vacancy-determined highly efficient oxygen reduction in NiCo2O4/hollow carbon spheres, ACS Appl. Mater. Interfaces 10 (2018) 16410–16417, https://doi.org/10.1021/acsami.8b01209.

[52] S. Khan, C. Wang, H. Lu, H. Cao, Z. Mao, C. Yan, X. Wang, In-situ tracking of phase conversion reaction induced metal/metal oxides for efficient oxygen evolution, Sci. China Mater. 64 (2020) 362–373, https://doi.org/10.1007/s40843-020-1424-2.

[53] M. Wang, Y. Cui, H. Cao, P. Wei, C. Chen, X. Li, J. Xu, G. Sheng, Activating peroxydisulfate with Co3O4/NiCo2O4 double-shelled nanocages to selectively degrade bisphenol A - A nonradical oxidation process, Appl. Catal. B Environ. 282 (2021), https://doi.org/10.1016/j.apcatb.2020.119585.

[54] X. Zou, J. Chen, Z. Rui, H. Ji, Sequential growth reveals multi-spinel interface promotion for methane combustion over alumina supported palladium catalyst, Appl. Catal. B Environ. 273 (2020), 119071, https://doi.org/10.1016/j.apcatb.2020.119071.

[55] Q. Hu, X. Huang, Z. Wang, G. Li, Z. Han, H. Yang, P. Liao, X. Ren, Q. Zhang, J. Liu, C. He, Slower removing ligands of metal organic frameworks enables higher electrocatalytic performance of derived nanomaterials, Small 16 (2020), 2002210, https://doi.org/10.1002/smll.202002210.

[56] Y. Song, Z. Li, K. Fan, Z. Ren, W. Xie, Y. Yang, M. Shao, M. Wei, Ultrathin layered double hydroxides nanosheets array towards efficient electrooxidation of 5-hydroxymethylfurfural coupled with hydrogen generation, Appl. Catal. B Environ. 299 (2021), 120669, https://doi.org/10.1016/j.apcatb.2021.120669.

[57] M.K. Bates, Q. Jia, H. Doan, W. Liang, S. Mukerjee, Charge-transfer effects in Ni-Fe and Ni-Fe-Co mixed-metal oxides for the alkaline oxygen evolution reaction, ACS Catal. 6 (2016) 155–161, https://doi.org/10.1021/acscatal.5b01481.

[58] J. Wu, Z. Ren, S. Du, L. Kong, B. Liu, W. Xi, J. Zhu, H. Fu, A highly active oxygen evolution electrocatalyst: Ultrathin CoNi double hydroxide/CoO nanosheets synthesized via interface-directed assembly, Nano Res. 9 (2016) 713–725, https://doi.org/10.1007/s12274-015-0950-4.

[59] D. Loche, C. Marras, D. Carta, M.F. Casula, G. Mountjoy, A. Corrias, Cation distribution and vacancies in nickel cobaltite, Phys. Chem. Chem. Phys. 19 (2017) 16775–16784, https://doi.org/10.1039/c7cp02260c.

[60] M. Cui, X. Ding, X. Huang, Z. Shen, T.-L. Lee, F.E. Oropeza, J.P. Hofmann, E.J. M. Hensen, K.H.L. Zhang, Ni3+-induced hole states enhance the oxygen evolution reaction activity of NixCo3–xO4 electrocatalysts, Chem. Mater. 31 (2019) 7618–7625, https://doi.org/10.1021/acs.chemmater.9b02453.

[61] C. Huang, Y. Huang, C. Liu, Y. Yu, B. Zhang, Integrating hydrogen production with aqueous selective semi-dehydrogenation of tetrahydroisoquinolines over a Ni2 P bifunctional electrode, Angew. Chem. Int. Ed. 58 (2019) 12014–12017, https://doi.org/10.1002/anie.201903327.

[62] Y. Huang, X. Chong, C. Liu, Y. Liang, B. Zhang, Boosting hydrogen production by anodic oxidation of primary amines over a NiSe Nanorod electrode, Angew. Chem. Int. Ed. 57 (2018) 13163–13166, https://doi.org/10.1002/anie.201807717.

[63] W. Chen, C. Xie, Y. Wang, Y. Zou, C.-L. Dong, Y.-C. Huang, Z. Xiao, Z. Wei, S. Du, C. Chen, B. Zhou, J. Ma, S. Wang, Activity origins and design principles of nickel-based catalysts for nucleophile electrooxidation, Chem 6 (2020) 2974–2993, https://doi.org/10.1016/j.chempr.2020.07.022.

[64] L. Gao, Z. Liu, J. Ma, L. Zhong, Z. Song, J. Xu, S. Gan, D. Han, L. Niu, NiSe@NiOx core-shell nanowires as a non-precious electrocatalyst for upgrading 5-hydroxy-methylfurfural into 2,5-furandicarboxylic acid, Appl. Catal. B Environ. 261 (2020) 118235, https://doi.org/10.1016/j.apcatb.2019.118235.

[65] H.-Y. Wang, Y.-Y. Hsu, R. Chen, T.-S. Chan, H.M. Chen, B. Liu, Ni3+-induced formation of active NiOOH on the spinel Ni-Co oxide surface for efficient oxygen evolution reaction, Adv. Energy Mater. 5 (2015), https://doi.org/10.1002/aenm.201500091.

[66] Z. Qiu, C.-W. Tai, G.A. Niklasson, T. Edvinsson, Direct observation of active catalyst surface phases and the effect of dynamic self-optimization in NiFe-layered double hydroxides for alkaline water splitting, Energy Environ. Sci. 12 (2019) 572–581, https://doi.org/10.1039/c8ee03282c.

[67] J. Li, J. Gong, Operando characterization techniques for electrocatalysis, Energy Environ. Sci. 13 (2020) 3748–3779, https://doi.org/10.1039/d0ee01706j.

[68] J. Wang, R. Gao, D. Zhou, Z. Chen, Z. Wu, G. Schumacher, Z. Hu, X. Liu, Boosting the electrocatalytic activity of Co3O4 nanosheets for a Li-O2 Battery through modulating inner oxygen vacancy and exterior Co3+/Co2+ ratio, ACS Catal. 7 (2017) 6533–6541, https://doi.org/10.1021/acscatal.7b02313.

[69] A. Moysiadou, S. Lee, C.S. Hsu, H.M. Chen, X. Hu, Mechanism of oxygen evolution catalyzed by cobalt oxyhydroxide: cobalt superoxide species as a key intermediate and dioxygen release as a rate-determining step, J. Am. Chem. Soc. 142 (2020) 11901–11914, https://doi.org/10.1021/jacs.0c04867.

[70] L. Reith, C.A. Triana, F. Pazoki, M. Amiri, M. Nyman, G.R. Patzke, Unraveling nanoscale cobalt oxide catalysts for the oxygen evolution reaction: maximum performance, minimum effort, J. Am. Chem. Soc. 143 (2021) 15022–15038, https://doi.org/10.1021/jacs.1c03375.

[71] J.A. Koza, C.M. Hull, Y.-C. Liu, J.A. Switzer, Deposition of β-Co(OH)2 films by electrochemical reduction of tris(ethylenediamine)cobalt(III) in alkaline solution, Chem. Mater. 25 (2013) 1922–1926, https://doi.org/10.1021/cm400579k.

[72] X. Han, C. Yu, S. Zhou, C. Zhao, H. Huang, J. Yang, Z. Liu, J. Zhao, J. Qiu, Ultrasensitive iron-triggered nanosized Fe-CoOOH integrated with graphene for highly efficient oxygen evolution, Adv. Energy Mater. 7 (2017), 1602148, https://doi.org/10.1002/aenm.201602148.

[73] W. Zhang, K. Lassen, C. Descorme, J.L. Valverde, A. Giroir-Fendler, Effect of the precipitation pH on the characteristics and performance of Co3O4 catalysts in the total oxidation of toluene and propane, Appl. B Environ. 282 (2021), 119566, https://doi.org/10.1016/j.apcatb.2020.119566.

[74] S. Mo, S. Li, Q. Ren, M. Zhang, Y. Sun, B. Wang, Z. Feng, Q. Zhang, Y. Chen, D. Ye, Vertically-aligned Co3O4 arrays on Ni foam as monolithic structured catalysts for CO oxidation: effects of morphological transformation, Nanoscale 10 (2018) 7746–7758, https://doi.org/10.1039/c8nr00147b.

[75] X. Chen, B. Liu, C. Zhong, Z. Liu, J. Liu, L. Ma, Y. Deng, X. Han, T. Wu, W. Hu, J. Lu, Ultrathin Co3O4 layers with large contact area on carbon fibers as high-performance electrode for flexible zinc-air battery integrated with flexible display, Adv. Energy Mater. 7 (2017), https://doi.org/10.1002/aenm.201700779.

[76] X. Lu, K.-H. Wu, B. Zhang, J. Chen, F. Li, B.-J. Su, P. Yan, J.-M. Chen, W. Qi, Highly efficient electro-reforming of 5-hydroxymethylfurfural on vertically oriented nickel nanosheet/carbon hybrid catalysts: structure-function relationships, Angew. Chem. Int. Ed. 60 (2021) 14528–14535, https://doi.org/10.1002/anie.202102359.

[77] J. Ren, K.-h Song, Z. Li, Q. Wang, J. Li, Y. Wang, D. Li, C.K. Kim, Activation of formyl C H and hydroxyl O H bonds in HMF by the CuO(1 1 1) and Co3O4(1 1 0) surfaces: a DFT study, Appl. Surf. Sci. 456 (2018) 174–183, https://doi.org/10.1016/j.apsusc.2018.06.120.

[78] X. Deng, X. Kang, M. Li, K. Xiang, C. Wang, Z. Guo, J. Zhang, X.-Z. Fu, J.-L. Luo, Coupling efficient biomass upgrading with H2 production via bifunctional CuxS@NiCo-LDH core-shell nanoarray electrocatalysts, J. Mater. Chem. A 8 (2020) 1138–1146, https://doi.org/10.1039/c9ta06917h.

[79] S. Barwe, J. Weidner, S. Cychy, D.M. Morales, S. Dieckhofer, D. Hiltrop, J. Masa, M. Muhler, W. Schuhmann, Electrocatalytic oxidation of 5-(hydroxymethyl) furfural using high-surface-area nickel boride, Angew. Chem. Int. Ed. 57 (2018) 11460–11464, https://doi.org/10.1002/anie.201806298.

[80] A.R. Poerwoprajitno, L. Gloag, J. Watt, S. Cychy, S. Cheong, P.V. Kumar, T. M. Benedetti, C. Deng, K.H. Wu, C.E. Marjo, D.L. Huber, M. Muhler, J.J. Gooding, W. Schuhmann, D.W. Wang, R.D. Tilley, Faceted branched nickel nanoparticles with tunable branch length for high-activity electrocatalytic oxidation of biomass, Angew. Chem. Int. Ed. Engl. 59 (2020) 15487–15491, https://doi.org/10.1002/anie.202005489.